

Article

# Integral Solution of Two-Region Solid–Liquid Phase Change in Annular Geometries and Application to Phase Change Materials–Air Heat Exchangers

Hamidreza Shabgard <sup>1,\*</sup>, Weiwei Zhu <sup>1</sup> and Amir Faghri <sup>2</sup>

<sup>1</sup> School of Aerospace and Mechanical Engineering, University of Oklahoma, 865 Asp Ave., Norman, OK 73019, USA; weiwei.zhu@ou.edu

<sup>2</sup> Department of Mechanical Engineering, University of Connecticut, 191 Auditorium Road, Storrs, CT 06269-3139, USA; amir.faghri@uconn.edu

\* Correspondence: shabgard@ou.edu; Tel.: +1-405-325-5753; Fax: +1-405-325-1088

Received: 2 October 2019; Accepted: 22 November 2019; Published: 24 November 2019



**Abstract:** A mathematical model based on the integral method is developed to solve the problem of conduction-controlled solid–liquid phase change in annular geometries with temperature gradients in both phases. The inner and outer boundaries of the annulus were subject to convective, constant temperature or adiabatic boundary conditions. The developed model was validated by comparison with control volume-based computational results using the temperature-transforming phase change model, and an excellent agreement was achieved. The model was used to conduct parametric studies on the effect of annuli geometry, thermophysical properties of the phase change materials (PCM), and thermal boundary conditions on the dynamics of phase change. For an initially liquid PCM, it was found that increasing the radii ratio increased the total solidification time. Also, increasing the Biot number at the cooled (heated) boundary and Stefan number of the solid (liquid) PCM, decreased (increased) the solidification time and resulted in a greater (smaller) solid volume fraction at steady state. The application of the developed method was demonstrated by design and analysis of a PCM–air heat exchanger for HVAC systems. The model can also be easily employed for design and optimization of annular PCM systems for all associated applications in a fraction of time needed for computational simulations.

**Keywords:** integral method; phase change materials; two-region phase change

## 1. Introduction

Phase change materials (PCM) can be found in a variety of applications, such as thermal insulation of building structures, cooling of electronic devices, waste heat recovery, energy storage, solar cooking and spacecraft thermal systems. The heat transfer associated with the solid–liquid phase change is difficult to analyze due to its transient nature and presence of moving phase boundary. In one classification, the solid–liquid phase change problems can be divided into two categories, namely the one-region and two-region problems [1]. In one-region problems, one of the phases remains at a constant temperature equal to the phase change temperature throughout the heat transfer process, whereas in two-region problem’s temperature gradients are established in both phases. The liquid and solid states of the PCM usually have different thermophysical properties, which adds to the difficulty of the solution procedure. A variety of solution methodologies have been developed for solid–liquid phase change problems. Analytical (exact) solutions have been studied extensively over several decades, but such methods are only available for certain moving boundary problems with simple geometries and initial and boundary conditions. Examples include one-region phase change in semi-infinite domain under constant temperature and constant heat flux boundary conditions [2,3].

Practical melting and solidification problems with greater levels of complexity should be solved using either approximate analytical methods or fully numerical techniques. Several approximate solution techniques have been developed including perturbation methods, heat balance integral technique, variational methods and quasi-stationary approximation. Rathjen and Jiji [4] presented an analytical solution to the two-dimensional solidification of a liquid filling the quarter space subject to a constant wall temperature. The solution was obtained by treating the heat of solidification as a moving heat source. A nonlinear, singular and integro-differential equation for the solid–liquid interface was derived and used to obtain the interface position. Jiji and Weinbaum [5] presented perturbation solutions for the problem of inward solidification in an annulus at an initial temperature different from the melting temperature. Kumar et al. [6] solved the outward radial melting of PCM contained in a spherical shell using variational, integral and quasi-steady methods. The PCM was initially at melting temperature and the inner surface was exposed to constant temperature boundary condition. Lamberg and Siren [7] presented a simplified analytical model to solve the melting process with a constant imposed end-wall temperature in a semi-infinite PCM storage. Jiji and Gaye [8] used a quasi-steady state approximation to examine the effect of volumetric heat generation in one-dimensional solidification and melting of a slab exposed to constant temperature boundary conditions. The transient term in the energy equation was neglected.

In a related study, Kalaiselvam et al. [9] studied the solidification and melting process of PCM inside cylindrical enclosures. The PCM was initially above melting temperature and exposed to constant temperature boundary conditions. Analytical solutions were obtained to find the interface locations at various time steps. Srivastava and Sinha [10] used the heat balance integral method to predict the interface location and temperature variation of PCM for melting in cylindrical and spherical cavity. The PCM was initially at fusion temperature and subject to constant temperature boundary condition on one wall and adiabatic boundary condition on the other wall. Mosaffa et al. [11] developed an approximate analytical model for the solidification process of PCM in a shell and tube finned thermal storage considering shells of circular and rectangular cross sections. Heat transfer fluid flowed in the inner tube and the outer storage surface was thermally insulated and the PCM was initially at melting point. Bechiri and Mansouri [12] analytically studied the volumetric heat generation effects during melting and solidification of nano-enhanced PCM in a horizontal cylindrical container subject to convection heat transfer on the outer boundary using the variables separation method and exponential integral function.

The integral method, proposed by Goodman [13], although approximate, provides an adequate accuracy for engineering purposes and simplifies the problem from one requiring the solution of partial differential equations to one requiring the solution of ordinary differential equations. Poots [14] used two approximate integral methods, the Karman–Pohlhausen method and Tani method, to solve the inward solidification of a uniform prism filled with liquid initially at melting temperature subject to constant temperature boundary conditions. Results were compared with data previously obtained from the relaxation method and showed good agreement for relatively large depth of solidification. Zhang and Faghri [15] studied the melting of PCM in an annular space in a thermal energy storage system using the integral method. Thermal energy was transferred to the PCM from a heat transfer fluid flowing in the inner cylinder. The PCM was initially at melting temperature and outer surface of the storage unit was thermally insulated. Siahpush and Crepeau [16] presented a solution for a one-dimensional phase change problem using the integral method for a semi-infinite domain with internal heat generation. The analysis assumed a quadratic temperature profile and a constant temperature boundary condition on the exposed surface.

Review of the literature shows a great amount of effort devoted to solving the solid–liquid phase change problems using analytical and semi-analytical methods. However, to the best of our knowledge, there are no analytical or semi-analytical methods for phase change in annular geometries involving heat transfer through both phases (two-region problem), under general boundary conditions. This effort presents an integral method to analyze the time dependent two-region conduction-controlled

melting and solidification of PCM in annular geometries subject to constant temperature or convective boundary conditions. The model provides accurate predictions of the transient evolution of the phase front location, as well as the temperature profiles within both solid and liquid phases. Compared with other analytical methods, the presented model in this work is simple and flexible to adapt to various types of boundary conditions. Furthermore, its flexibility and fast response time allows for simple design and optimization of PCM heat exchangers.

## 2. Mathematical Model

The geometry of the problem considered in this work is shown in Figure 1. The PCM was contained in an annular region and was assumed to be initially liquid at melting temperature  $T_m$ . The inner and outer radii of the annulus were  $r_i$  and  $r_o$ , respectively. At time  $t = 0$ , the inner boundary at  $r = r_i$  was exposed to convective heating by a hot fluid at temperature  $T_h$  (above the melting point) and a heat transfer coefficient  $h_i$ , while the outer boundary was subjected to convective cooling by a cold fluid at  $T_c$  (below the melting point) and a heat transfer coefficient  $h_o$ . The thermophysical properties of the PCM were assumed to be constant and different for the solid and liquid phases.

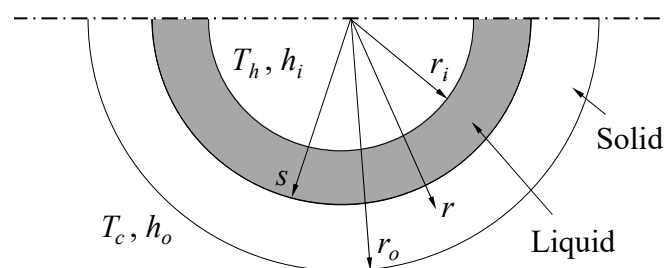


**Figure 1.** Cross-sectional view of the annular geometry subject to convective heat and cooling.

In order to overcome the relatively small thermal conductivity of most of the common phase change materials, the PCM was assumed to be embedded within a porous solid matrix, such as metal foams and expanded graphite, for enhanced heat transfer. Such high conductivity porous solid matrices have attracted widespread interest in PCM applications due to their significant impact on increasing the heat transfer rates [17,18]. It has been well established that the presence of the solid foams effectively suppresses the natural convection within the melt and leads to a conduction-controlled melting [19–21]. To this end, the present model considers conduction-controlled melting. Based on these assumptions, the energy equations for the solid and liquid regions of the PCM can be written as [1]:

$$\frac{1}{\alpha_{liq}} \frac{\partial T_{liq}}{\partial t} = \frac{1}{r} \frac{\partial}{\partial r} \left( r \frac{\partial T_{liq}}{\partial r} \right) \quad r_i < r < s \quad (1)$$

$$\frac{1}{\alpha_{sol}} \frac{\partial T_{sol}}{\partial t} = \frac{1}{r} \frac{\partial}{\partial r} \left( r \frac{\partial T_{sol}}{\partial r} \right) \quad s < r < r_o \quad (2)$$

where  $s$  shows the location of the solid–liquid interface measured from the center of the annulus, and subscripts *liq* and *sol* denote the liquid and solid phases, respectively. The inner and outer convective boundary conditions are:

$$-k_{liq} \frac{\partial T_{liq}}{\partial r} = h_i (T_h - T_{liq}) \quad r = r_i \quad (3)$$

$$-k_{sol} \frac{\partial T_{sol}}{\partial r} = h_o (T_{sol} - T_c) \quad r = r_o \quad (4)$$

The energy balance and temperature continuity at the interface are:

$$\rho_{liq} h_{sl} \frac{ds}{dt} = k_{sol} \frac{\partial T_{sol}}{\partial r} - k_{liq} \frac{\partial T_{liq}}{\partial r} \quad r = s \quad (5)$$

$$T_{liq}(r, t) = T_{sol}(r, t) = T_m \quad r = s \quad (6)$$

where  $h_{sl}$  and  $T_m$  are the PCM heat of fusion and the fusion temperature, respectively. To apply the integral solution, the following dimensionless variables are defined:

$$\begin{aligned} \theta_{liq} &= \frac{T_{liq} - T_m}{T_h - T_m} & \theta_{sol} &= \frac{T_{sol} - T_m}{T_m - T_c} & R &= \frac{r}{r_i} & R_o &= \frac{r_o}{r_i} & S &= \frac{s}{r_i} & \tau &= \frac{\alpha_{liq} t}{r_i^2} \\ Ste_{liq} &= \frac{c_{liq}(T_h - T_m)}{h_{sl}} & Ste_{sol} &= \frac{c_{sol}(T_m - T_c)}{h_{sl}} & Bi_{liq} &= \frac{h_i r_i}{k_{liq}} & Bi_{sol} &= \frac{h_o r_i R_o}{k_{sol}} \\ N_k &= \frac{k_{sol}}{k_{liq}} & N_c &= \frac{c_{sol}}{c_{liq}} & N_\alpha &= \frac{\alpha_{sol}}{\alpha_{liq}} \end{aligned}$$

where  $\theta$ ,  $R$ ,  $S$ , and  $\tau$  are the dimensionless variables for temperature, radial coordinate, phase front location, and time, respectively,  $Ste$  denotes the Stefan number and  $Bi$  indicates the Biot number. Also,  $c$ ,  $k$ ,  $\alpha$  and  $h$  represent the specific heat, thermal conductivity, thermal diffusivity, and heat transfer coefficient, respectively. The dimensionless temperatures are defined in such a way that  $0 \leq \theta_{liq} \leq 1$  and  $-1 \leq \theta_{sol} \leq 0$ , and both are zero at the phase interface, where the temperature is equal to  $T_m$ . Using the above dimensionless variables, Equations (1) to (6) can be nondimensionalized as following:

$$\frac{\partial \theta_{liq}}{\partial \tau} = \frac{1}{R} \frac{\partial}{\partial R} \left( R \frac{\partial \theta_{liq}}{\partial R} \right) \quad 1 < R < S \quad (7)$$

$$\frac{1}{N_\alpha} \frac{\partial \theta_{sol}}{\partial \tau} = \frac{1}{R} \frac{\partial}{\partial R} \left( R \frac{\partial \theta_{sol}}{\partial R} \right) \quad S < R < R_o \quad (8)$$

$$\frac{\partial \theta_{liq}}{\partial R} = Bi_{liq} (\theta_{liq} - 1) \quad R = 1 \quad (9)$$

$$\frac{\partial \theta_{sol}}{\partial R} = -Bi_{sol} (\theta_{sol} + 1) \frac{1}{R_o} \quad R = R_o \quad (10)$$

$$\frac{dS}{d\tau} = \frac{N_k}{N_c} Ste_{sol} \frac{\partial \theta_{sol}}{\partial R} - Ste_{liq} \frac{\partial \theta_{liq}}{\partial R} \quad R = S \quad (11)$$

$$\theta_{liq}(R, \tau) = \theta_{sol}(R, \tau) = 0 \quad R = S \quad (12)$$

Logarithmic temperature profiles have been shown to satisfy the governing equations and boundary conditions associated with phase change in annular geometries [15]. The following logarithmic dimensionless temperature distributions for the solid and liquid phases are employed:

$$\theta_{liq} = A + B \left( \frac{\ln R}{\ln S} \right) - (A + B) \left( \frac{\ln R}{\ln S} \right)^2 \quad (13)$$

$$\theta_{sol} = -C - D \frac{\ln(R/R_o)}{\ln(S/R_o)} + (C + D) \left[ \frac{\ln(R/R_o)}{\ln(S/R_o)} \right]^2 \quad (14)$$

where  $A$ ,  $B$ ,  $C$  and  $D$  are the four time-dependent variables to be determined by satisfying Equations (7)–(12).

It is noted that when the interface velocity is very large, such as very early stage of phase change adjacent to a wall with a large heat transfer rate, the temperature profiles of Equations (13) and (14) fail to capture the temperature distribution due to the excessively sharp slope close to the interface. It was found that for such conditions, first degree logarithmic functions of the form  $\theta_{liq} = C_1 + C_2 (\ln R / \ln S)$  and  $\theta_{sol} = C_3 + C_4 \ln(R/R_o) \ln(S/R_o)^{-1}$  were able to capture the highly transient large heat fluxes. The constants  $C_1$  to  $C_4$  were easily determined by application of the boundary and interfacial conditions. However, for all other times, the temperature profiles of Equations (13) and (14) provided significantly more accurate results. For the cases that required the first degree logarithmic temperature profiles

(i.e., two-region phase change with constant temperature wall), it was found that the total time period where these functions were needed was about 1% of the total duration of the phase change.

By differentiating Equations (13) and (14) and applying boundary conditions (9) to (12), the following equations were obtained:

$$\frac{\partial \theta_{liq}}{\partial R} = \frac{B \ln S - 2(A + B) \ln R}{R(\ln S)^2} \quad (15)$$

$$\frac{\partial^2 \theta_{liq}}{\partial R^2} = -\frac{B \ln S + 2(A + B)(1 - \ln R)}{R^2(\ln S)^2} \quad (16)$$

$$\frac{\partial \theta_{liq}}{\partial R} \Big|_{R=1} = \frac{B}{\ln S} \quad (17)$$

$$\frac{\partial \theta_{liq}}{\partial R} \Big|_{R=S} = -\frac{2A + B}{S \ln S} \quad (18)$$

$$\frac{\partial^2 \theta_{liq}}{\partial R^2} \Big|_{R=S} = \frac{(B + 2A) \ln S - 2(A + B)}{S^2(\ln S)^2} \quad (19)$$

$$\frac{\partial \theta_{sol}}{\partial R} = \frac{-D \ln(S/R_0) + 2(C + D) \ln(R/R_0)}{R[\ln(S/R_0)]^2} \quad (20)$$

$$\frac{\partial^2 \theta_{sol}}{\partial R^2} = \frac{D \ln(S/R_0) + 2(C + D)[1 - \ln(R/R_0)]}{R^2[\ln(S/R_0)]^2} \quad (21)$$

$$\frac{\partial \theta_{sol}}{\partial R} \Big|_{R=R_0} = -\frac{D}{R_0 \ln(S/R_0)} \quad (22)$$

$$\frac{\partial \theta_{sol}}{\partial R} \Big|_{R=S} = \frac{2C + D}{S \ln(S/R_0)} \quad (23)$$

$$\frac{\partial^2 \theta_{sol}}{\partial R^2} \Big|_{R=S} = \frac{-(2C + D) \ln(S/R_0) + 2(C + D)}{S^2[\ln(S/R_0)]^2} \quad (24)$$

Substituting Equation (17) into Equation (9), and Equation (22) into Equation (10), a relation between  $A$  and  $B$ , as well as between  $C$  and  $D$  could be obtained as follows:

$$B = (A - 1)Bi_{liq} \ln S \quad (25)$$

$$D = (1 - C)Bi_{sol} \ln(S/R_0) \quad (26)$$

Differentiating  $\theta_{liq}$  in Equation (12) yields:

$$d\theta_{liq} = \frac{\partial \theta_{liq}}{\partial R} dR + \frac{\partial \theta_{liq}}{\partial \tau} d\tau = 0, \quad R = S \quad (27)$$

which can be rearranged to get:

$$\frac{\partial \theta_{liq}}{\partial R} \frac{dS}{d\tau} + \frac{\partial \theta_{liq}}{\partial \tau} = 0, \quad R = S \quad (28)$$

Combining Equations (7) and (28) yields:

$$\frac{\partial \theta_{liq}}{\partial R} \frac{dS}{d\tau} + \frac{1}{R} \frac{\partial \theta_{liq}}{\partial R} + \frac{\partial^2 \theta_{liq}}{\partial R^2} = 0, \quad R = S \quad (29)$$

Substituting Equations (11), (18), and (19) into Equation (29), a quadratic function of  $A$  and  $B$  could be obtained:

$$Ste_{liq}(2A + B)^2 + \left(\frac{N_k}{N_c}\right) \frac{\ln S}{\ln(S/R_o)} Ste_{sol}(2A + B)(2C + D) + 2(A + B) = 0 \quad (30)$$

Similar expressions as Equations (27) to (29) can be derived for  $\theta_{sol}$ , resulting in a quadratic function of  $C$  and  $D$ :

$$N_k N_c Ste_{sol}(2C + D)^2 + \frac{\ln(S/R_o)}{\ln S} Ste_{liq}(2A + B)(2C + D) + 2N_\alpha(C + D) = 0 \quad (31)$$

Equations (25), (26), (30) and (31) represent a system of four coupled nonlinear equations with four unknown variables  $A$ ,  $B$ ,  $C$  and  $D$ . This system of equations is solved numerically. The solution procedure is described in Section 2.2.

### 2.1. Special Case of Constant Temperature Boundaries

Constant temperature boundary conditions can be viewed as convective boundary with infinite heat transfer coefficient ( $Bi \rightarrow \infty$ ). Considering Equations (25) and (26) in the limiting case of  $Bi \rightarrow \infty$ , the only way for  $B$  and  $D$  to have finite values is that  $A$  and  $C$  are equal to 1. Thus, the dimensionless temperature distributions in the solid and liquid phases under the constant temperature boundary conditions are:

$$\theta_{liq} = 1 + B \left(\frac{\ln R}{\ln S}\right) - (1 + B) \left(\frac{\ln R}{\ln S}\right)^2 \quad (32)$$

$$\theta_{sol} = -1 - D \frac{\ln(R/R_o)}{\ln(S/R_o)} + (1 + D) \left[\frac{\ln(R/R_o)}{\ln(S/R_o)}\right]^2 \quad (33)$$

The constants  $A = 1$  and  $C = 1$  can then be substituted into Equations (30) and (31) to convert them into a system of two equations and two unknowns. For a given  $S$ , this system can be solved for  $B$  and  $D$  to obtain the temperature distributions and phase front displacement rate.

### 2.2. Solution Procedure

This section describes the step-by-step procedure to solve for the evolution of the phase front location,  $S$ , and time-dependent temperature profiles across the solid and liquid PCM regions. The required input includes seven nondimensional variables, namely  $Bi_{liq}$ ,  $Bi_{sol}$ ,  $Ste_{liq}$ ,  $Ste_{sol}$ ,  $R_o$ ,  $N_k$ ,  $N_c$ , and  $N_\alpha$ , as well as the initial location of the phase interface,  $S_0$ . The solution starts with an initial guessed value for  $A$ . Using the initial values for  $S$  and  $A$ ,  $B$  is found from Equation (25), and Equations (30) and (31) are converted into a system of two algebraic equations with two unknowns that can be solved to obtain  $C$  and  $D$ . Replacing the calculated value of  $C$  in Equation (26) results in a second value for  $D$ . A *residual* is defined as the difference between the two values of  $D$  obtained from Equation (26) and from the solution of Equations (30) and (31). If the absolute value of the residual is greater than a selected convergence criterion, the initial value of  $A$  is varied and the above procedure is repeated until the residual approaches zero within an acceptable range ( $<10^{-6}$  in the present work). It is noted that the changes to  $A$  are made in a systematic manner based upon the variations of the residual in the past iterations according to the bisection method [22].

Once  $A$ ,  $B$ ,  $C$ , and  $D$  corresponding to the provided interface location  $S$  are determined, they can be substituted into Equations (18) and (23) and replaced into Equation (11) to determine the displacement rate of the interface:

$$\frac{dS}{d\tau} = \frac{N_k}{N_c} Ste_{sol} \frac{2C + D}{S \ln(S/R_o)} + Ste_{liq} \frac{2A + B}{S \ln S} \quad (34)$$

Next, the phase front location is advanced using the velocity calculated from the Equation (34);  $S(\tau + \Delta\tau) = S(\tau) + dS/d\tau (\Delta\tau)$ , where  $\Delta\tau$  is the time step to march in time. In the new time step,  $S(\tau)$  is replaced by  $S(\tau + \Delta\tau)$  and the above solution procedure is repeated. The marching in time continues until the steady-state is reached or the phase change is completed. For the results presented in this work, a time step size of  $\Delta\tau = 0.001$  was found to yield results that were independent of the time step size.

### 3. Validation

The integral solution was validated by comparison with computational results obtained from a control volume code based on the temperature transforming method [1]. Validation studies of the code against experimental results has been reported in prior publications by one of the authors [23,24]. Due to the conduction-controlled phase change, the momentum and pressure correction equations were deactivated in the computational model and only the energy equation was solved:

$$\rho \frac{\partial(cT)}{\partial t} = \frac{1}{r} \frac{\partial}{\partial r} \left( kr \frac{\partial T}{\partial r} \right) - \rho \frac{\partial se}{\partial t} \quad (35)$$

The specific heat,  $c$ , and the source term,  $se$ , appearing in the above equation are defined as a function of temperature:

$$c(T) = \begin{cases} c_{sol}, & T < T_m - \delta T \\ \left( \frac{c_{sol} + c_{liq}}{2} \right) + \frac{h_{sl}}{2\delta T}, & T_m - \delta T < T < T_m + \delta T \\ c_{liq}, & T > T_m + \delta T \end{cases} \quad (36)$$

$$se(T) = \begin{cases} c_{sol}\delta T, & T < T_m - \delta T \\ \left( \frac{c_{sol} + c_{liq}}{2} \right) \delta T + \frac{h_{sl}}{2}, & T_m - \delta T < T < T_m + \delta T \\ c_{liq}\delta T, & T > T_m + \delta T \end{cases} \quad (37)$$

where  $\delta T$  is a small temperature defining the mushy zone. For the results presented here, a  $\delta T$  of  $0.01^\circ\text{C}$  was employed. The above equations were solved using an in-house finite volume computer code implemented in FORTRAN. A detailed study was performed to establish the grid and time step size independency of the computational results. For this study, the computational model was employed to determine the temporal evolution of the solid volume fraction during freezing process of a PCM in an annulus with  $R_o = 4$ . The solid and liquid Stefan numbers were set to 0.2 and 0.3, respectively. Before starting the freezing process, steady-state temperature profile was established in fully melted PCM by setting the temperature at the outer boundary equal to the melting temperature ( $\theta = 0$ ) and subjecting the inner boundary to convective heating with  $Bi = 4$ . The freezing process was triggered by changing the outer boundary temperature to  $\theta_{sol} = -1$ . In each time step, the solution was considered converged when the residual of the energy equation decreased to less than  $10^{-9}$ . Figure 2a,b show the variations of the solid volume fraction with time for various grid sizes and time steps, respectively. In these figures, a zoomed-in inset is included to show the effect of the studied variable in further detail. From the results, a grid size of 100 cells in radial direction and a time step size of 10 s were found to provide results that were independent of the computational grid and time step size.

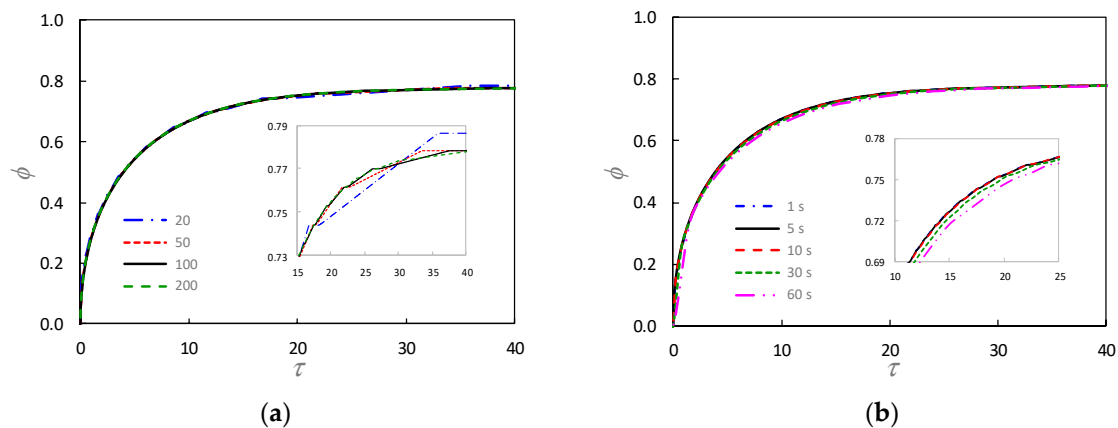


**Figure 2.** Study of the effect of (a) grid size in radial direction, and (b) the time step size on the phase change materials' solid volume fraction during freezing process.

For the validation studies of the integral method, the PCM properties and the boundary conditions in the numerical model were set to match the nondimensional parameters used in the integral solution. After the simulations were completed, the numerical results were converted to nondimensional form for comparison with the results from the integral method. Comparisons were made for 5 combinations of boundary conditions shown in Table 1. In case (a), the inner and outer boundaries were subject to constant temperatures above and below the melting temperature, respectively. In case (b), the inner boundary was convectively heated and the outer boundary was at a constant temperature smaller than the melting temperature. For the third case (c), the inner boundary was adiabatic ( $Bi = 0$ ) and the outer boundary was at constant temperature below the melting temperature. In case (d), the inner and outer boundaries were subject to convective heating and cooling, respectively. Finally, in case (e), the inner boundary was adiabatic and the outer boundary was convectively cooled. The dimensionless outer radius  $R_o$  was kept constant at 4 and the Stefan number of the solid and liquid phases were set to 0.2 and 0.3, respectively. The initial condition for all the cases was fully melted PCM. The initial temperature distribution was the steady-state temperature profile obtained by applying an inner boundary condition from Table 1 and an outer boundary temperature of  $\theta = 0$  (for cases (c) and (e), the initial condition reduces to liquid PCM at  $\theta = 0$ ).

**Table 1.** Boundary conditions for validation cases.

Case	Inner Boundary Condition	Outer Boundary Condition
(a)	constant temperature, $Bi \rightarrow \infty$	constant temperature, $Bi \rightarrow \infty$
(b)	convection, $Bi = 4$	constant temperature, $Bi \rightarrow \infty$
(c)	adiabatic, $Bi = 0$	constant temperature, $Bi \rightarrow \infty$
(d)	convection, $Bi = 4$	convection, $Bi = 4$
(e)	adiabatic, $Bi = 0$	convection, $Bi = 4$

The results of the solid phase volume fraction  $\phi$  calculated by integral and numerical methods are shown in Figure 3. In this figure, the symbols represent the results from the integral method and the numerical results are represented by lines. For all cases, an excellent agreement was achieved between the results obtained from the integral and numerical methods with a discrepancy of less than 1%. The simulations were carried out on a PC with Intel Core i5 processor and 8 GB of RAM. For all the five cases, the solution time for the integral model was less than 5 s, whereas the solution time for the finite volume model varied from about 30 s for case (c) to about 120 s for case (d), showing a substantial reduction in computational cost. The reduction in computational time will be more profound for systems involving multiple PCM units. For example, the case study presented in Section 5 includes 30 rows of convectively cooled PCM units that must be analyzed consecutively. The integral model solved the benchmark problem presented in Section 5 in less than 2 min. A finite volume model would

have taken more than 1 h to solve the same problem. The time saving offered by the integral model becomes particularly advantageous for optimization and parametric studies of latent heat thermal energy storage systems, where a large number of design conditions must be explored.

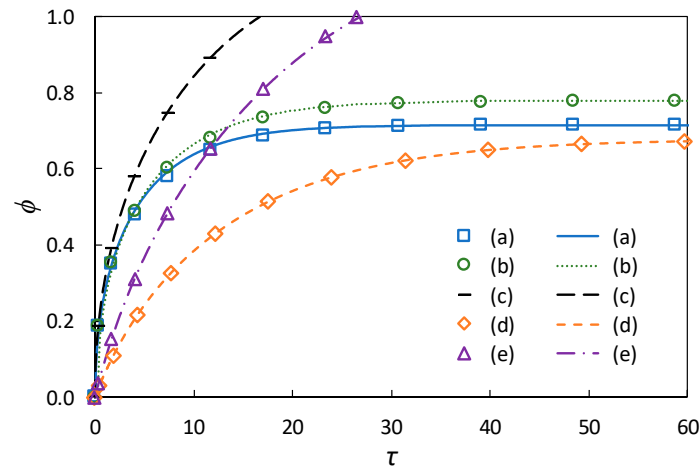


**Figure 3.** Comparison of the integral and computational methods for five combinations of boundary conditions; symbols represent results from the integral method and lines represent computational results: (a) constant temperature inner boundary and constant temperature outer boundary, (b) convective inner boundary and constant temperature outer boundary, (c) adiabatic inner boundary and constant temperature outer boundary, (d) convective inner boundary and convective outer boundary, and (e) adiabatic inner boundary and convective outer boundary.

#### 4. Results and Discussion

Parametric studies were carried out to investigate the effects of the five important dimensionless design and operational parameters, namely the annuli radius ratio  $R_o$ , Biot numbers at the heated and cooled boundaries, and Stefan numbers of the solid and liquid phases, on the heat transfer behavior of the PCM. The results were compared with a base case in which the radii ratio was set to  $R_o = 4$ , the inner and outer boundaries were subject to convective heating and cooling, respectively, with  $Bi = 4$ , and the Stefan number of 0.3 was applied to both solid and liquid phases. In each of the five parametric studies, only one parameter was varied while the other four remained unchanged. For all the cases,  $N_k$ ,  $N_c$ , and  $N_\alpha$  were equal to 1.

##### 4.1. Effect of Dimensionless Radius $R_o$

To investigate the effect of the radii ratio, the solidification of initially melted PCM in annuli with three values of  $R_o$  of 2, 4, and 8 was studied. All other parameters including the solid and liquid Stefan numbers and Biot numbers at the heated and cooled walls were the same as the base case. Table 2 summarizes the operating and boundary conditions for the three cases. Figure 4 shows the solid volume fraction development with time for the three cases. It can be observed that the annular space with the greatest radii ratio took the longest time to complete solidification. A four times increase in the radius ratio from  $R_o = 2$  to  $R_o = 8$  resulted in about 13 times increase in the dimensionless times for the phase change to reach steady state ( $\tau \approx 15$  for  $R_o = 2$  and  $\tau \approx 200$  for  $R_o = 8$ ). The dimensionless temperature distributions at steady state are shown in Figure 5. The liquid and solid regions are represented by solid and dashed lines, respectively. It can be seen that the temperature at the inner (outer) boundary was closer to 1 (-1) for greater radii ratios. From Equations (9) and (10), the smaller temperature difference at the boundaries corresponds to smaller temperature slopes at the boundaries that is evident in Figure 5. Considering the smaller temperature gradients at the inner boundary ( $R = 1$ ) for greater radii ratios, and noting the equality of the input and output heat transfer rates at

steady state, it can be inferred from Figure 5 that the steady state heat transfer rate through the PCM decreased when the radii ratio increased.

**Table 2.** Parametric study on the effect of radii ratio on phase change in annulus.

Parameters	Base Case	Variations	
		(v1)	(v2)
$R_o$	4	2	8
$Bi_{sol}$	4	4	4
$Bi_{liq}$	4	4	4
$Ste_{sol}$	0.3	0.3	0.3
$Ste_{liq}$	0.3	0.3	0.3

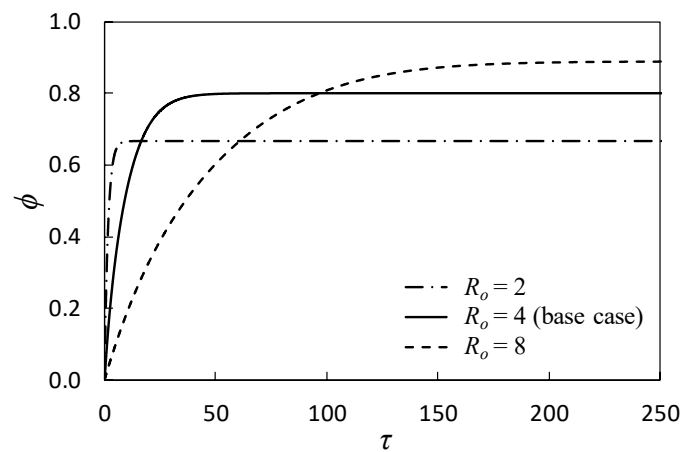


**Figure 4.** Solid volume fraction evolution with time for various annuli with various ratios of outer rad.

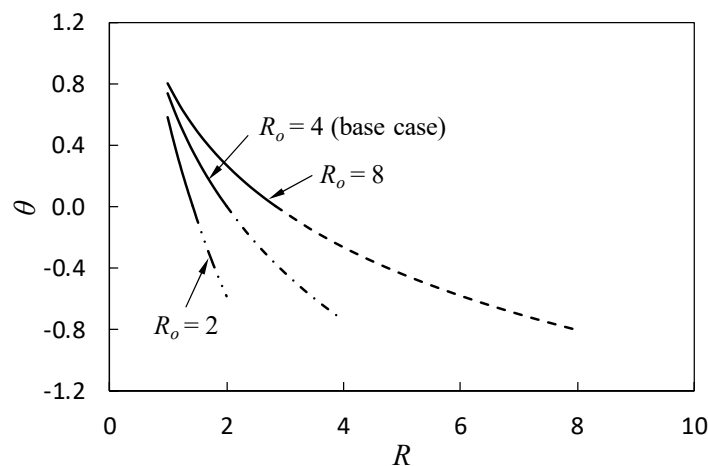


**Figure 5.** Nondimensional temperature distribution of the solid and liquid phases at steady state for various ratios of outer to inner radius to inner radius.

#### 4.2. Effect of Biot Number

This section investigates the effect of Biot number on the phase change behavior of the PCM. Table 3 lists the details of the four cases where Biot numbers were changed and compared with the base case. Cases (v1) and (v2) are the parametric studies of the Biot number at the outer boundary where PCM is cooled,  $Bi_{sol}$ . In case (v1),  $Bi_{sol}$  is set to 2, half of that in the base case, and in case (v2),  $Bi_{sol}$  is set to 8, double that in the base case. In cases (v3) and (v4), the Biot number at the inner boundary adjacent to liquid PCM,  $Bi_{liq}$ , is varied to 2 and 8 while  $Bi_{sol}$  remains unchanged.

**Table 3.** Parametric study on the effect of Biot number on the phase change in annulus.

Parameters	Base Case	Variations			
		(v1)	(v2)	(v3)	(v4)
$R_o$	4	4	4	4	4
$Bi_{sol}$	4	2	8	4	4
$Bi_{liq}$	4	4	4	2	8
$Ste_{sol}$	0.3	0.3	0.3	0.3	0.3
$Ste_{liq}$	0.3	0.3	0.3	0.3	0.3

Figure 6 shows the solid volume fraction variations with time for various  $Bi_{sol}$  and  $Bi_{liq}$  values. As shown in Figure 6a, the dimensionless time for the phase change to reach steady state was about 100, 60 and 40 when  $Bi_{sol}$  was 2, 4 and 8, respectively. As expected, increasing the Biot number at the cooling boundary decreased the total solidification time and resulted in a greater solid volume fraction at steady state. Figure 6b shows the evolution of the solid volume fraction with time for  $Bi_{liq}$  equal to 2, 4 and 8 at constant  $Bi_{sol} = 4$ . The total solidification time was about 60, 50 and 40 for  $Bi_{liq}$  of 2, 4 and 8, respectively. The greater  $Bi_{liq}$  values decreased the total solid volume fraction at steady state due to higher heat transfer rates to the interface from the liquid side. Also, due to the improved heat transfer rates from the liquid side, steady-state was reached in a slightly shorter time. Figure 7 shows the effect of Biot number on the dimensionless temperature profiles at steady state. It is evident in this figure that when  $Bi_{sol}$  ( $Bi_{liq}$ ) was increased, the outer (inner) surface temperature decreased (increased), leading to a sharper temperature gradient and shorter time to reach steady state.

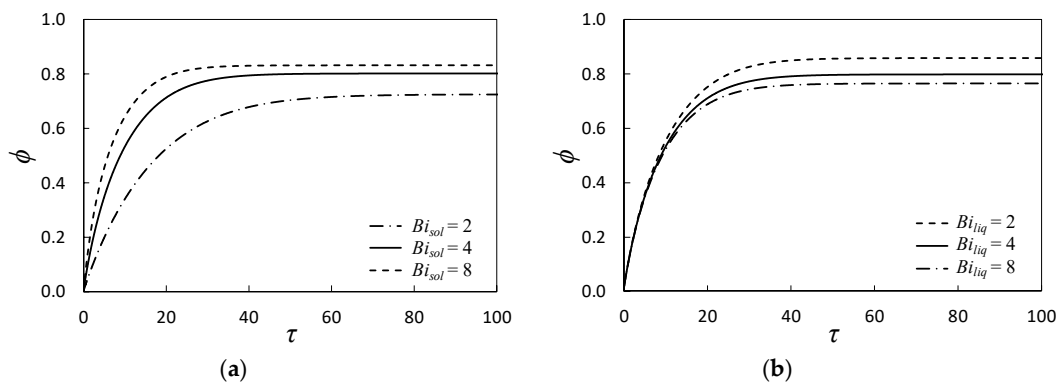


**Figure 6.** Overall solid volume fraction variations with time for (a) varying  $Bi_{sol}$  and constant  $Bi_{liq}$ , and (b) varying  $Bi_{liq}$  and constant  $Bi_{sol}$ .

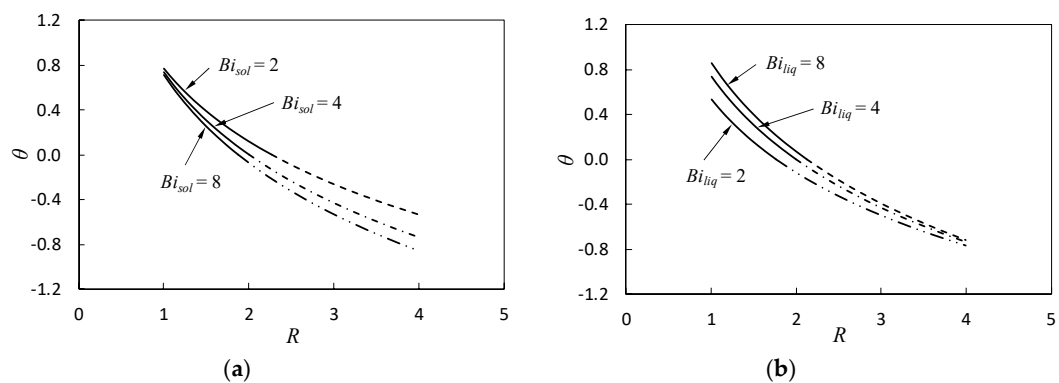


**Figure 7.** Nondimensional temperature distribution of the solid and liquid phases at steady state for (a) varying  $Bi_{sol}$  and constant  $Bi_{liq}$ , and (b) varying  $Bi_{liq}$  and constant  $Bi_{sol}$ .

### 4.3. Effect of Stefan Number

In this section, the effect of Stefan number on the PCM phase change behavior is studied. Table 4 lists the details of the parametric study. In cases (v1) and (v2), the Stefan number of the solid phase,  $Ste_{sol}$ , was varied to 0.1 and 0.5 and compared with the base case with  $Ste_{sol} = 0.3$ . Cases (v3) and (v4) are related to liquid Stefan numbers,  $Ste_{liq}$ , of 0.1, 0.3 (base case) and 0.5. Figure 8 shows the solid volume fraction development from parametric study of  $Ste_{sol}$  and  $Ste_{liq}$ . As shown in Figure 8a, the total dimensionless solidification time was about 100, 60 and 30 for  $Ste_{sol}$  of 0.1, 0.3 and 0.5, respectively. In Figure 8b, the total solidification time was about 30, 50, and 70 for  $Ste_{liq}$  of 0.1, 0.3 and 0.5, respectively. Figure 8 shows that increasing  $Ste_{sol}$  and/or decreasing  $Ste_{liq}$  increased the solid volume fraction at steady state. When the material properties are constant, the increase in Stefan number can be viewed as greater temperature difference between the heating or cooling source and the melting temperature. Thus, greater  $Ste_{sol}$  ( $Ste_{liq}$ ) corresponds to greater driving temperature difference for solidification (melting), which in turn led to greater (smaller) solid volume fraction at steady state. Moreover, when  $Ste_{sol}$  was increased ( $Ste_{liq}$  was decreased), the greater solid volume fractions at steady-state were also reached in a shorter time.

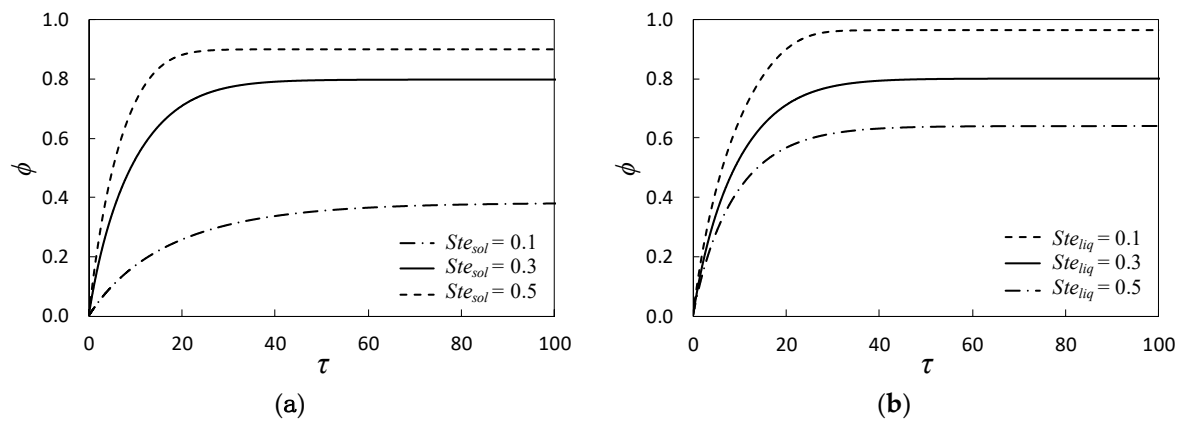


**Figure 8.** Solid volume fraction variations with time for (a) varying  $Ste_{sol}$  and constant  $Ste_{liq}$ , and (b) varying  $Ste_{liq}$  values and constant  $Ste_{sol}$ .

**Table 4.** Parametric study on the effect of Stefan number on phase change in annulus.

Parameters	Base Case	Variations			
		(v1)	(v2)	(v3)	(v4)
$R_o$	4	4	4	4	4
$Bi_{sol}$	4	4	4	4	4
$Bi_{liq}$	4	4	4	4	4
$Ste_{sol}$	0.3	0.1	0.5	0.3	0.3
$Ste_{liq}$	0.3	0.3	0.3	0.1	0.5

Figure 9 shows the dimensionless temperature distribution from parametric study of  $Ste_{sol}$  and  $Ste_{liq}$ . It is evident that increasing  $Ste_{sol}$  and/or decreasing  $Ste_{liq}$  led to smaller surface temperatures. The steady state dimensionless temperature profiles in Figure 9 have different slopes adjacent to the interface in the solid and liquid regions. This is because of the nondimensionality. The actual solid and liquid steady-state temperature profiles have the same exact slope at the interface considering similar thermal conductivities and steady-state conditions (see Equation (5) with  $ds/dt$  set to 0).

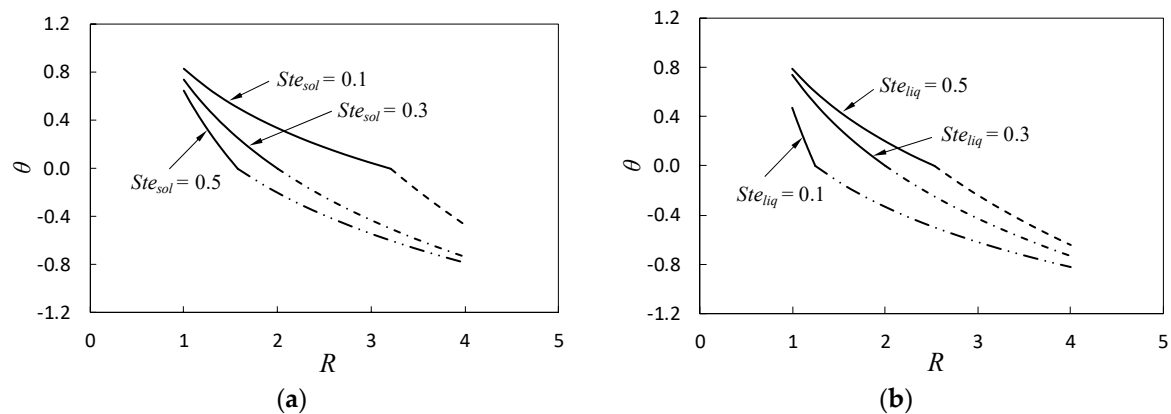


**Figure 9.** Nondimensional temperature distribution of the solid and liquid phases at steady state for (a) varying  $Ste_{sol}$  values and constant  $Ste_{liq}$ , and (b) varying  $Ste_{liq}$  values and constant  $Ste_{sol}$ .

## 5. Application

The application of the developed integral method is demonstrated by design and analysis of a sample solar PCM–air heat exchanger. The solar PCM–air heat exchanger can be incorporated into an air handler unit to partially cover the heating needs for supplying warm air to a building space in winter nights using the solar thermal energy stored during the daytime. The heat exchanger is comprised of a series of concentric pipes arranged in a staggered tube bundle (Figure 10a). The annular space between the inner and outer pipes is filled with a PCM. The PCM is melted during the day by warm water flowing through the inner pipes. The warm water can be supplied by a simple flat plate solar water heater. During the night, cold fresh air from outside flows over the outer pipes and preheats by absorbing heat from the solidifying PCM.

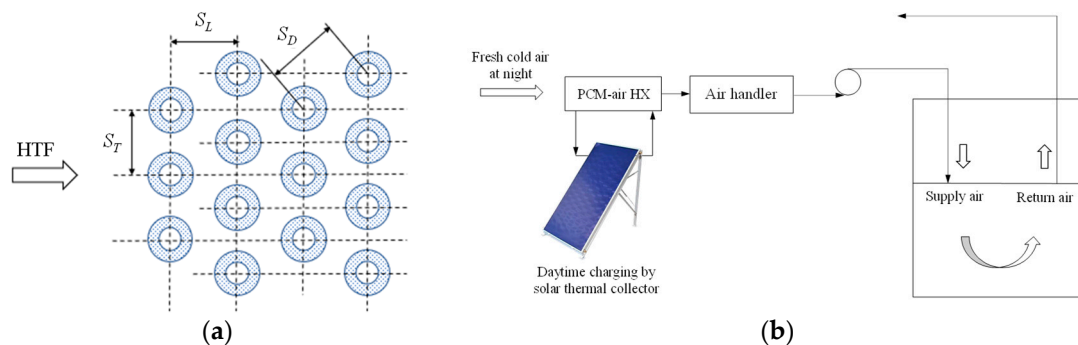


**Figure 10.** (a) Configuration of the tube bundle, and (b) schematic of the HVAC system integrated with the solar PCM–air heat exchanger.

The heat exchanger is assumed to include 30 rows of cylinders with 10 cylinders in each row (a total of 300 cylinders). The cylinders are assumed to be 1-m long and have inner and outer diameters of 0.01 m and 0.04 m, respectively. The transverse and longitudinal spacing of the cylinders in the tube bundle are  $S_T = 0.05$  m and  $S_L = 0.043$  m, respectively. The average heat transfer coefficient associated with the flow of cold air over the bundle can be calculated from Zukauskas correlation [25]. Commercial PCM PureTemp 37) from PureTemp® (PureTemp LLC, Minneapolis, MN, USA) [26] was used in the analysis. Thermal properties of PureTemp 37 are listed in Table 5. The density change of the PCM upon phase change was neglected. As seen in the table, the PCM has a low thermal conductivity that hinders effective heat transfer. To this end, the PCM is assumed to be embedded in aluminum foam for heat transfer enhancement. The aluminum foam is assumed to have a porosity of 97.7%, creating a PCM-metal foam composite with an effective thermal conductivity of 2 W/m·K. Details of the calculation of the effective thermal conductivity can be found elsewhere [27]. It is noted that this

case study did not aim to optimize the design of the PCM–air heat exchanger and is mainly intended to demonstrate the application of the developed model for time-efficient analysis of engineering systems.

**Table 5.** Thermal properties of PureTemp 37<sup>®</sup> PCM.

Melting Temperature (°C)	Heat of Fusion (kg/kJ)	Thermal Conductivity (W/m·K)	Density (kg/m <sup>3</sup> )	Specific Heat (kJ/kg·K)
37	210	0.25 (solid)	920 (solid)	2.21 (solid)
		0.15 (liquid)	840 (liquid)	2.63 (liquid)

Only the discharging (freezing) process of the PCM is considered. It is assumed that the PCM was fully melted during the day and the discharge process started with liquid PCM at the melting temperature. The discharge process includes both latent heat transfer from the solidifying PCM and sensible heat transfer from the completely solidified PCM. During the latter stage, heat transfer takes place from relatively warmer solid PCM to the relatively colder intake air. The sensible heat transfer diminishes when the temperature of the solid PCM approaches that of the intake air. The integral method described in Section 2 is employed to analyze the problem in the phase change stage. The heat transfer analysis during cooling of the fully solidified PCM is described in the Appendix A.

For the heat transfer analysis, the length of the PCM–air heat exchanger was divided into a number of elements, each including one row of cylinders (a total of 30 elements in this case). During a time step, the air temperature was assumed to remain constant within each element. The analysis started from the first element for which the inlet air temperature was known. The air temperature was applied as the cold source temperature in the integral method and the temperature of the outer surface of the PCM,  $T_o$ , was determined from the model. In each time step, the heat transfer from the PCM to the air was calculated from  $q = hA(T_o - T_{air})$ . Having the heat transfer  $q$ , the temperature rise of the air across the element was calculated from  $T_{air,out} = T_{air,in} + q / (\dot{m}_{air}c_{p,air})$ . The calculations were then moved to the next time step for the same element. The heat transfer analysis of the first element continued until the PCM was completely solidified and the temperature of the solid PCM approached the inlet air temperature. The analysis of the first element determines the transient variations of the air temperature at the outlet of the element for the entire duration of solidification and the following sensible cooling. The outlet temperature from the first element was used as the inlet temperature to the second element. A similar procedure was repeated for the second element, with the inlet temperature being the outlet temperature of the first element. The solution progressed through the downstream elements until the entire length of the heat exchanger was covered.

The inlet air temperature and velocity were varied to study their impact on the outlet air temperature from the PCM–air heat exchanger. Figure 11 shows the results of the thermal performance of the PCM–air heat exchanger for various air inlet velocities at a constant inlet temperature of 0 °C. Three air inlet velocities of 1 m/s, 0.5 m/s and 0.3 m/s, were considered. Figure 11a shows the temporal variations of the outlet air temperature. Two distinct stages can be observed in the outlet temperature profiles; a relatively stable initial stage followed by a sharply decreasing stage. The first stage is related to the time period where the majority of the rows still possess some molten PCM and as such their temperature is anchored to the fusion temperature of the PCM. In the latter stage, the majority of the rows are completely solidified and their temperature drops quickly as they release heat to the air. Figure 11b depicts the evolution of the overall solid volume fraction with time throughout the entire PCM heat exchanger. The overall solid volume fractions were calculated by averaging the solid volume fractions of all the 30 rows in each time step. As evident, increasing the air velocity decreased the solidification time. An almost linear relationship was observed between the air velocity and the total solidification time. It was also observed that in all cases the solid volume fraction increased almost linearly with time except the final stage of solidification.

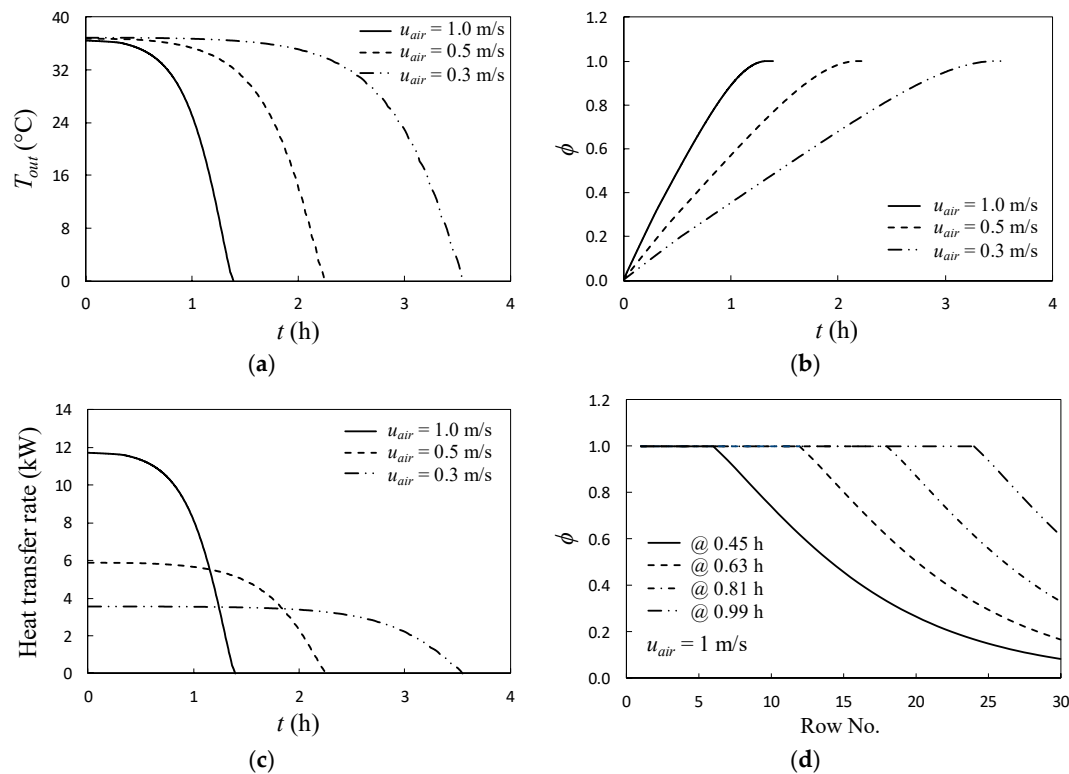


**Figure 11.** Time variations of (a) the air outlet temperature, (b) the overall solid volume fraction throughout the PCM heat exchanger, and (c) heat transfer rate during the phase change process for various air inlet velocities. (d) Snapshots of solid volume fraction distribution across the tube bundle for an air inlet velocity of 1 m/s.

Figure 11c shows the total heat transfer rate during the phase change process. As evident, the heat transfer rate was fairly constant during the early stage of solidification. The relatively stable heat transfer rate was attributed to presence of multiple rows of the PCM; when an upstream row was fully solidified, the heat transfer from the following row automatically increased due to greater temperature difference. It could also be observed that reducing the inlet air velocity resulted in a longer period of stable heat transfer rate. Figure 11d shows snapshots of the solid volume fraction across the entire tube bundle at certain times during the solidification process. As shown, the PCM in the tube rows closer to the air inlet solidified faster than the downstream rows due to exposure to colder air. In the downstream elements, the air was already preheated that led to smaller temperature differences and smaller heat transfer rates from the PCM.

Figure 12 shows the results of the heat exchanger's thermal performance for three inlet air temperatures of 0 °C, 5 °C and 10 °C and a constant inlet velocity of 0.3 m/s. For each case, the simulation was stopped when the outlet air temperature dropped to about 0.1 °C above the air inlet temperature. It could be observed in Figure 12a that for relatively greater air inlet temperatures, the outlet temperature could be maintained relatively stable for a longer period of time. The same two heat transfer stages discussed with regard to Figure 11a were also observed in Figure 12a. Figure 12b shows the effect of the air inlet temperature on the overall solid volume fraction throughout the entire PCM heat exchanger. As evident, decreasing the air inlet temperature decreased the solidification time. Quantitatively, every 5 °C increase in the air inlet temperature increased the solidification time by about 0.5 h. Figure 12c shows the heat transfer rate during the entire discharge period (including both latent and sensible heat transfer stages). As evident, increasing the air inlet temperature resulted in a longer period of relatively constant heat transfer rate. A 5 °C increase in the air inlet temperature decreased the heat transfer rates by about 500 W during the first stage of heat transfer. Figure 12d shows the distribution of the solid volume fraction across the entire tube bundle at certain times during

the operation for an inlet air temperature of 10 °C. Again, the full solidification started at the rows closer to the inlet and progressed toward the downstream rows as the time elapsed.

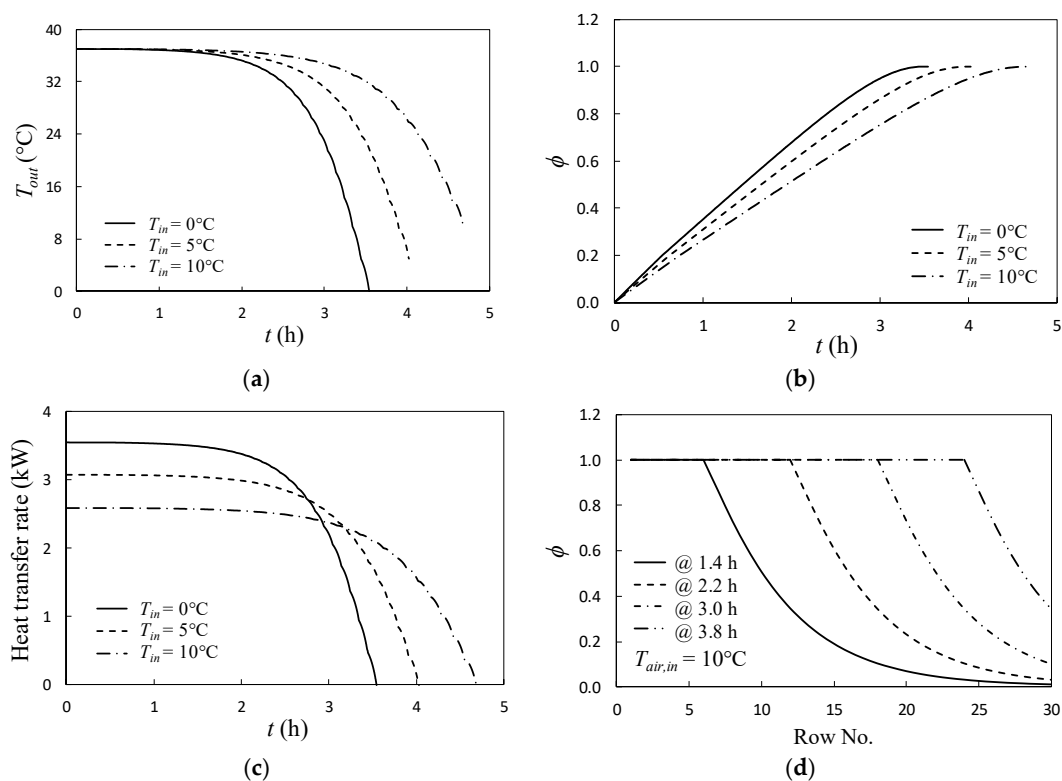


**Figure 12.** Time variations of (a) air outlet temperature, (b) the overall solid volume fraction throughout the PCM heat exchanger, and (c) heat transfer rate during the phase change process for various air inlet temperatures. (d) Snapshots of solid volume fraction distribution across the tube bundle for an inlet air temperature of 10 °C.

## 6. Conclusions

A semianalytical model based on the integral method was developed to solve the two-region melting and solidification of PCM in annuli. The inner and outer boundaries of the annulus could be subject to convective, constant temperature or adiabatic boundary conditions. The model was validated by comparison with a control volume-based computational model that employed the temperature-transforming method to capture the phase change. The results of the integral model deviated from the computational results by less than 1%. The developed model was employed to conduct parametric studies on the effect of the radii ratio,  $R_o$ , Biot numbers at the heated and cooled boundaries,  $Bi_{liq}$  and  $Bi_{sol}$ , and Stefan numbers of the liquid and solid phases,  $Ste_{liq}$  and  $Ste_{sol}$ , respectively. It was found that increasing the radii ratio increased the total solidification time. Increasing  $Bi_{sol}$  or  $Ste_{sol}$  and decreasing  $Bi_{liq}$  or  $Ste_{liq}$  both led to a reduced solidification time and a larger solid volume fraction at steady state. The analytical model was applied to analyze the performance of a solar PCM–air heat exchanger for applications in heating, ventilation and air conditioning (HVAC). It was demonstrated that a properly designed PCM–air heat exchanger, could serve as an auxiliary heater for the air handler and reduce energy consumption. More than one order of magnitude reduction in the computational time was achieved by using the integral model as compared to finite volume simulations. The significantly smaller computational cost offered by the present model is particularly attractive for optimization and parametric studies of latent heat thermal energy storage systems, where a large number of design conditions must be explored.

**Author Contributions:** Conceptualization, H.S.; methodology, H.S. and A.F.; software, H.S. and W.Z.; validation, A.F.; formal analysis, W.Z.; investigation, A.F.; resources, H.S. and A.F.; data curation, W.Z.; writing—original draft preparation, H.S. and W.Z.; writing—review and editing, A.F.; visualization, W.Z.; supervision, H.S. and A.F.; project administration, H.S.; funding acquisition, H.S.

**Funding:** Support from the Advanced Research Projects Agency-Energy under Award Number DE-AR0001069 is acknowledged and appreciated. Support from the Gallogly College of Engineering at the University of Oklahoma is also appreciated.

**Conflicts of Interest:** The authors declare no conflict of interest.

## Nomenclature

$A$	time-dependent variable
$B$	time-dependent variable
$Bi$	Biot number
$C$	time-dependent variable
$c$	specific heat (J/kg·K)
$D$	time-dependent variable
$h$	heat transfer coefficient (W/m <sup>2</sup> ·K)
$h_{sl}$	heat of fusion (J/kg)
$k$	thermal conductivity (W/m·K)
$N_c$	specific heat ratio
$N_k$	thermal conductivity ratio
$N_\alpha$	thermal diffusivity ratio
$R$	dimensionless radial coordinate
$r$	radial coordinate, or radius (m)
$S$	dimensionless phase front location
$s$	phase front location (m)
$se$	energy source term
$Ste$	Stefan number
$t$	time (s)
$T$	temperature (°C)
$T_m$	fusion temperature (°C)

## Greek

$\alpha$	thermal diffusivity (m <sup>2</sup> /s)
$\phi$	volume fraction
$\theta$	dimensionless temperature
$\rho$	density (kg/m <sup>3</sup> )
$\tau$	Fourier number

## Subscripts

$c$	cold
$h$	hot
$i$	inner boundary
$liq$	liquid
$o$	outer boundary
$sol$	solid

## Appendix A : Integral Solution of Sensible Heat Transfer

After solidification is completed, the average temperature of the PCM may be greater than the air flowing over it. This temperature difference induces heat transfer from solid PCM to the air. The heat transfer in the completely solidified PCM is governed by Equation (2) subject to convective cooling at the outer surface and adiabatic inner boundary. This problem can be solved analytically using the integral transform method [28]. However, a simpler integral solution is developed here to provide a unified and consistent integral method to capture all the stages of heat transfer to or from the PCM.

The inner and outer boundary conditions are represented by:

$$\frac{\partial \theta_{sol}}{\partial R} = 0 \quad R = 1 \quad (A1)$$

$$-R_o \frac{\partial \theta_{sol}}{\partial R} = Bi_{sol}(\theta_{sol} + 1) \quad R = R_o \quad (A2)$$

where  $\theta_{sol} = (T - T_m)/(T_m - T_f)$ , with  $T_f$  being the heat transfer fluid temperature adjacent to the PCM. The following nondimensional temperature profile is used in which the coefficients  $E$ ,  $F$  and  $G$  are a function of time only:

$$\theta_{sol} = E + F \ln R + G \ln^2 R \quad (A3)$$

Application of the boundary condition (A1) yields  $F = 0$ , and boundary condition (A2) provides a relation between  $E$  and  $G$ :

$$E = -G \left( \ln^2 R_o + \frac{2 \ln R_o}{Bi_{sol}} \right) - 1 \quad (A4)$$

Temperature profile (A3) can be rewritten using Equation (A4) as follows:

$$\theta_{sol} = -G \left( \ln^2 R_o - \ln^2 R + \frac{2 \ln R_o}{Bi_{sol}} \right) - 1 \quad (A5)$$

The dependency of  $G$  on time can be obtained from the following transient energy balance applied to unit length of the annulus:

$$m c_{sol} \frac{d\bar{T}_{sol}}{dt} = 2\pi r_o k \left. \frac{\partial T_{sol}}{\partial r} \right|_{r_o} \quad (A6)$$

where  $m$  and  $\bar{T}_{sol}$  are the mass and mass-averaged temperature of the solid PCM, respectively. The above equation can be represented in the following nondimensional form:

$$(R_o^2 - 1) \frac{d\bar{\theta}_{sol}}{d\tau} = 2R_o \left. \frac{\partial \theta_{sol}}{\partial R} \right|_{R_o} \quad (A7)$$

The dimensionless average temperature can be obtained by integrating the temperature profile of (A3) from  $R = 1$  to  $R = R_o$ :

$$\bar{\theta}_{sol} = \frac{2}{R_o^2 - 1} \int_1^{R_o} \theta_{sol} R dR = \frac{G}{R_o^2 - 1} \left[ \ln^2 R_o + \left( \frac{2}{Bi_{sol}} - R_o^2 - \frac{2R_o^2}{Bi_{sol}} \right) \ln R_o + \frac{R_o^2 - 1}{2} \right] - 1 \quad (A8)$$

Substituting  $\bar{\theta}_{sol}$  from Equation (A8) into Equation (A7) and noting that  $(\partial \theta_{sol} / \partial R)|_{R_o} = (2G \ln R_o) / R_o$ , the following equation is obtained:

$$\frac{dG}{d\tau} \left[ \ln R_o + \frac{2}{Bi_{sol}} - R_o^2 - \frac{2R_o^2}{Bi_{sol}} + \frac{R_o^2 - 1}{2 \ln R_o} \right] = 4G \quad (A9)$$

The above equation can be integrated to obtain  $G$  as a function of dimensionless time:

$$G = C_1 \exp \left[ \frac{8 Bi_{sol} \ln R_o}{2 Bi_{sol} \ln^2 R_o + 4 \ln R_o - 2R_o^2 \ln R_o (Bi_{sol} + 2) + Bi_{sol} (R_o^2 - 1)} \tau \right] \quad (A10)$$

The constant of integration,  $C_1$ , can be found from the initial condition; at the beginning of the sensible cooling stage, when the solidification process was just completed, the temperature at the inner adiabatic boundary is equal to the melting temperature:

$$\theta_{sol}(R = 1, \tau = 0) = 0 \quad (A11)$$

Substituting  $G$  from Equation (A10) into Equation (A5) and applying Equation (A11), the constant  $C_1$  can be found as following:

$$C_1 = - \frac{Bi_{sol}}{Bi_{sol} \ln^2 R_o + 2 \ln R_o} \quad (A12)$$

The nondimensional temperature during the sensible cooling as a function of time and space can be found by substituting the Equations (A10) and (A12) into Equation (A5):

$$\theta_{sol} = -1 - C_1 \left( \ln^2 R_o - \ln^2 R + \frac{2 \ln R_o}{Bi_{sol}} \right) \exp \left[ \frac{8 Bi_{sol} \ln R_o}{2 Bi_{sol} \ln^2 R_o + 4 \ln R_o - 2 R_o^2 \ln R_o (Bi_{sol} + 2) + Bi_{sol} (R_o^2 - 1)} \tau \right] \quad (A13)$$

## References

1. Faghri, A.; Zhang, Y. *Transport Phenomena in Multiphase Systems*; Academic Press: Cambridge, MA, USA, 2006.
2. El-Genk, M.S.; Cronenberg, A.W. Solidification in a semi-infinite region with boundary conditions of the second kind: An exact solution. *Lett. Heat Mass Transf.* **1979**, *6*, 321–327. [[CrossRef](#)]
3. Bechiri, M.; Mansouri, K. Exact solution of thermal energy storage system using PCM flat slabs configuration. *Energy Convers. Manag.* **2013**, *76*, 588–598. [[CrossRef](#)]
4. Rathjen, K.A.; Jiji, L.M. Heat Conduction with Melting or Freezing in a Corner. *J. Heat Transf.* **1971**, *93*, 101. [[CrossRef](#)]
5. Jiji, L.M.; Weinbaum, S. Perturbation solutions for melting or freezing in annular regions initially not at the fusion temperature. *Int. J. Heat Mass Transf.* **1978**, *21*, 581–592. [[CrossRef](#)]
6. Kumar, A.; Prasad, A.; Upadhaya, S.N. Spherical phase-change energy storage with constant temperature heat injection. *J. Energy Resour. Technol.* **1987**, *109*, 101–104. [[CrossRef](#)]
7. Lamberg, P.; Sirén, K. Analytical model for melting in a semi-infinite PCM storage with an internal fin. *Heat Mass Transf.* **2003**, *39*, 167–176. [[CrossRef](#)]
8. Jiji, L.M.; Gaye, S. Analysis of solidification and melting of PCM with energy generation. *Appl. Therm. Eng.* **2006**, *26*, 568–575. [[CrossRef](#)]
9. Kalaiselvam, S.; Veerappan, M.; Aaron, A.A.; Iniyar, S. Experimental and analytical investigation of solidification and melting characteristics of PCMs inside cylindrical encapsulation. *Int. J. Therm. Sci.* **2008**, *47*, 858–874. [[CrossRef](#)]
10. Srivastava, M.; Sinha, M.K. Heat balance integral method for cylindrical and spherical encapsulated phase change thermal energy storage system. *Int. J. Mech. Eng. Technol.* **2017**, *8*, 890–898.
11. Mosaffa, A.H.; Talati, F.; Tabrizi, H.B.; Rosen, M.A. Analytical modeling of PCM solidification in a shell and tube finned thermal storage for air conditioning systems. *Energy Build.* **2012**, *49*, 356–361. [[CrossRef](#)]
12. Bechiri, M.; Mansouri, K. Analytical study of heat generation effects on melting and solidification of nano-enhanced PCM inside a horizontal cylindrical enclosure. *Appl. Therm. Eng.* **2016**, *104*, 779–790. [[CrossRef](#)]
13. Goodman, T.R. The heat-balance integral and its application to problems involving a change of phase. *Trans. ASME J. Heat Transf.* **1958**, *80*, 335.
14. Poots, G. On the application of integral-methods to the solution of problems involving the solidification of liquids initially at fusion temperature. *Int. J. Heat Mass Transf.* **1962**, *5*, 525–531. [[CrossRef](#)]
15. Zhang, Y.; Faghri, A. Semi-analytical solution of thermal energy storage system with conjugate laminar forced convection. *Int. J. Heat Mass Transf.* **1996**, *39*, 717–724. [[CrossRef](#)]
16. Siahpush, A.; Crepeau, J. Integral Solutions of Phase Change with Internal Heat Generation. In Proceedings of the 12th International Conference on Nuclear Engineering, Arlington, VA, USA, 25–29 April 2004; pp. 339–344. [[CrossRef](#)]
17. Qureshi, Z.A.; Ali, H.M.; Khushnood, S. Recent advances on thermal conductivity enhancement of phase change materials for energy storage system: A review. *Int. J. Heat Mass Transf.* **2018**, *127*, 838–856. [[CrossRef](#)]
18. Chen, X.; Li, X.; Xia, X.; Sun, C.; Liu, R. Thermal Performance of a PCM-Based Thermal Energy Storage with Metal Foam Enhancement. *Energies* **2019**, *12*, 3275. [[CrossRef](#)]
19. Tian, Y.; Zhao, C.Y. A numerical investigation of heat transfer in phase change materials (PCMs) embedded in porous metals. *Energy* **2011**, *36*, 5539–5546. [[CrossRef](#)]
20. Li, W.Q.; Qu, Z.G.; He, Y.L.; Tao, W.Q. Experimental and numerical studies on melting phase change heat transfer in open-cell metallic foams filled with paraffin. *Appl. Therm. Eng.* **2012**, *37*, 1–9. [[CrossRef](#)]
21. Wang, G.; Wei, G.; Xu, C.; Ju, X.; Yang, Y.; Du, X. Numerical simulation of effective thermal conductivity and pore-scale melting process of PCMs in foam metals. *Appl. Therm. Eng.* **2019**, *147*, 464–472. [[CrossRef](#)]

22. Chapra, S.C.; Canale, R.P. *Numerical Methods for Engineers*, 7th ed.; McGraw-Hill Education: New York, NY, USA, 2014.
23. Wang, S.; Faghri, A.; Bergman, T.L. A comprehensive numerical model for melting with natural convection. *Int. J. Heat Mass Transf.* **2010**, *53*, 1986–2000. [[CrossRef](#)]
24. Sharifi, N.; Bergman, T.L.; Allen, M.J.; Faghri, A. Melting and solidification enhancement using a combined heat pipe, foil approach. *Int. J. Heat Mass Transf.* **2014**, *78*, 930–941. [[CrossRef](#)]
25. Bergman, T.L.; Lavine, A.S.; Incropera, F.P.; DeWitt, D.P. *Fundamentals of Heat and Mass Transfer*, 7th ed.; Wiley: Hoboken, NJ, USA, 2011.
26. PureTemp—Global Authority on Phase Change Material. Available online: <http://www.puretemp.com> (accessed on 2 October 2019).
27. Shabgard, H.; Song, L.; Zhu, W. Heat transfer and exergy analysis of a novel solar-powered integrated heating, cooling, and hot water system with latent heat thermal energy storage. *Energy Convers. Manag.* **2018**, *175*, 121–131. [[CrossRef](#)]
28. Özisik, M.N. *Heat Conduction*; Wiley: Hoboken NJ, USA, 1993; Available online: [https://books.google.com/books/about/Heat\\_Conduction.html?id=WyZRAAAAMAAJ](https://books.google.com/books/about/Heat_Conduction.html?id=WyZRAAAAMAAJ) (accessed on 22 March 1993).



© 2019 by the authors. Licensee MDPI, Basel, Switzerland. This article is an open access article distributed under the terms and conditions of the Creative Commons Attribution (CC BY) license (<http://creativecommons.org/licenses/by/4.0/>).